JTTEE5 17:887–894
DOI: 10.1007/s11666-008-9268-z
1059-9630/$19.00 © ASM International

A Comparative Microstructural Investigation of Nanostructured and Conventional Al_2O_3 Coatings Deposited by Plasma Spraying

D. Zois, A. Lekatou, M. Vardavoulias, I. Panagiotopoulos, and A. Vazdirvanidis

(Submitted June 12, 2008; in revised form September 19, 2008)

Nanostructured and conventional Al_2O_3 powders have been plasma sprayed to produce coatings. The parameters for retaining a fraction of the nanostructure were investigated. Dissimilarities were observed between the two types of coating, regarding properties and phase proportions, which are related with the different percentages of semimolten particles in the coatings. The nanocoatings retained a higher percentage of semimolten particles than the conventional coatings owing to the higher porosity of the nanoparticle agglomerates. The molten part of both conventional and nanostructured coatings consisted of γ-Al_2O_3 of columnar morphology. In order to investigate the mechanism of the melting front advance into the particle interior, the particles were sprayed directly into deionized water. The nanoparticles mainly formed hollow spheres, whereas the conventional particles mainly formed compact spheres. The internal porosity of the solidified nanoparticle agglomerates, which affected the overall coating porosity and, consequently, coating properties such as hardness, adhesion, and surface roughness, was linked to the hollow sphere phenomenon.

Keywords APS coatings, influence of spray parameters, nanopowders, nanostructured coatings, porosity of coatings

1. Introduction

Nanocrystalline bulk materials (having a grain size smaller than 100 nm) are experiencing a rapid development in recent years due to their existing and/or potential applications to a wide variety of technological areas, such as electronics, catalysis, ceramics, magnetic data storage, structural components, etc. As the grain size is reduced to the nanometer range, materials exhibit peculiar and interesting mechanical and physical properties, e.g. increased mechanical strength, enhanced diffusivity, higher specific heat and electrical resistivity, in comparison with conventional coarse-grained counterparts. Nanostructured bulk materials and coatings are reported to demonstrate superior resistance to wear, erosion, cracking, and spallation (Ref 1-3).

Thermal spraying has recently been employed to prepare nanostructured coatings (Ref 4-8). Plasma sprayed ceramic coatings using nanostructured powder feed have been deposited and studied. Nanostructured titania and alumina-titania coatings have been obtained by vacuum plasma and atmospheric plasma spraying (APS) (Ref 9-12). Nanostructured zirconia has also been APS deposited (Ref 13). Certain conditions have to prevail for retaining a portion of the original nanostructure in the coating during the spraying process, thus maintaining the beneficial properties of the nanostructure. The retained nanostructure in the coatings is considered to be the decisive factor for the enhancement of the mechanical properties. Works have shown that nanostructured thermal spray ceramic oxide coatings like Al_2O_3-TiO_2 can have superior wear performance when compared to similar coatings produced from conventional ceramic oxide powder (Ref 1, 14). However, Liu et al. (Ref 15) have not observed this same improvement in the wear behavior when using nanostructured feedstocks, but they observed dependence on the spray method applied. Dependence of the mechanical properties on the spraying technique and the nanostructure feedstock has been suggested by Lima and Marple (Ref 16). Besides the retained nanostructure (depending on proper spraying conditions), the coating must have integrity, stability, and adhesion on the substrate, which can be attained by a sufficient degree of particle melting.

This article is an invited paper selected from presentations at the 2008 International Thermal Spray Conference and has been expanded from the original presentation. It is simultaneously published in *Thermal Spray Crossing Borders, Proceedings of the 2008 International Thermal Spray Conference*, Maastricht, The Netherlands, June 2-4, 2008, Basil R. Marple, Margaret M. Hyland, Yuk-Chiu Lau, Chang-Jiu Li, Rogerio S. Lima, and Ghislain Montavon, Ed., ASM International, Materials Park, OH, 2008.

D. Zois and **M. Vardavoulias**, Pyrogenesis SA, Technological Park of Lavrion, 19500 Lavrion, Greece; **D. Zois, A. Lekatou,** and **I. Panagiotopoulos**, Department of Materials Science and Engineering, University of Ioannina, 45111 Ioannina, Greece; and **A. Vazdirvanidis**, Hellenic Centre for Metal Research, Pireos 252, 17778 Athens, Greece. Contact e-mail: dzois@pyrogenesis-sa.gr.

In the present study, the factors for achieving the above-mentioned requirements are examined for a High Energy Ball Milled nanostructured alumina powder. Moreover, an effort is made to associate the melting degree of the powder with the portions of the phases present in the deposited coating and its metallographic properties. A conventional counterpart is used for comparison reasons.

Here, it should be noted that this study was induced by the Pyrogenesis SA need to produce coatings for fiber and thread wear resistant applications at high temperatures. These coatings should possess excellent wear behavior and excellent erosion resistance at high temperatures. Up to now, the raw material for these coatings is conventional Al_2O_3 powder.

2. Experimental

The Al_2O_3 nanopowder, hereafter named NP, employed in this work was composed of agglomerated nanoparticles, in order to enable the flow, through the powder feeder, into the torch (Ref 17). The powder was produced by a high-energy ball mill manufactured by MBN and functioning according to the kinematic characteristics of a Spex® 8000 model (Ref 18). After milling, the powder was centrifugally classified to exclude particles finer than 10 μm. Rounder particle shapes were obtained by low energy milling (Jet Mill). Finally, the appropriate particle distribution for spraying was attained by mechanical sieving. No heat treatment process was used. The received powder's nominal size distribution was (−53 + 10) μm. The conventional powder, hereafter named CP, was Sulzer Metco's Al_2O_3-105NS of (−45 + 15) μm particle distribution. The powders were sprayed by a MiniGun torch with an external powder feeder developed by Pyrogenesis Inc. The substrates used were 50 × 50 × 5 mm 304 stainless steel coupons.

The apparent porosity and thickness of the coatings were evaluated by optical microscopy (Leica DM4000M) and scanning electron microscopy (Philips XL 40 SFEG). Microhardness was measured by a Shimadzu tester (average of 14 measurements on each coating) using a load of 0.1 kg for 10 s. The fracture toughness of the coatings was qualitatively examined by indentation with a 1.0 kg load. The adhesion strength of the coatings (average of three measurements on each coating) was measured by a portable elcometer (110 P.A.T.T.I.®). Surface roughness was determined by a TR200 Roughness tester. The phase composition of the feedstocks and coatings was established by X-ray diffraction (XRD) (Bruker D8 Advance, Standard Slit). XRD was also employed to estimate the average crystal size of the feedstocks and coatings (Ref 19, 20). The crystal size and lattice strain in the coatings can be determined by the X-ray broadening techniques, since XRD peaks are broadened due to three factors: (i) instrumental effects, (ii) small crystal size, and (iii) lattice strain in the material (Ref 21). The instrumental effects were measured and subtracted by diffracting a SiO_2 standard. The crystal size was determined by the use of Williamson-Hall equation (Ref 22):

$$D = \frac{K\lambda}{\beta_{size}\cos\theta} + 2\varepsilon\sin\theta \qquad \text{(Eq 1)}$$

where D is the crystal size in Å, $K = 0.9$, β_{size} the peak width in rad, λ the wavelength of the X-ray radiation in Å, θ the Bragg angle, and ε is the internal strain ($\varepsilon = \Delta d/d$, where d is the lattice spacing and Δd the lattice strain).

The X-ray Rietveld Method was applied to determine the phase percentages in the original powders and their coatings by refining the crystalline parameters and scale factors (Ref 23). The software used was PowderCell v2.4.

3. Results

3.1 Feedstock Characterization

The morphologies of the conventional (CP) and nanostructured (NP) feedstocks are shown in Fig. 1(a) and (b), respectively. CP is in the form of solid granules due to the fusing and crushing manufacturing process, whereas NP is in the form of agglomerates of irregular spherical shapes. Individual nanoparticles on the surface of the agglomerated granules can be discerned in Fig. 1(c). Figure 2 shows that the main phase in both powders is α-Al_2O_3. NP also contains some iron. Probably, the powder was contaminated by the tool steel balls and vials of the high-energy ball mill. The percentage of iron was estimated by EDS analysis to be ~0.74 wt.%, while by Rietveld analysis it was estimated to be 1.14 wt.%.

In Fig. 2, NP presents broader peaks than the conventional powder due to nanocrystalline dimensions and presence of non-uniform strain. The strain originates from the consecutive high-energy impacts during the milling process introducing high stress and distortion into the grains. The calculated strain was 1.15%. The estimated crystal size of the nanostructured powder was 105 nm.

3.2 Thermal Spraying as a Function of the Torch Power

The effect of the torch power on characteristic coating properties (microporosity, surface roughness, microhardness, adhesion, and crack propagation resistance) was investigated by conducting three series of spraying experiments. The series are characterized as low (25 kW, coatings obtained designated as C_1 and N_1, conventional and nanostructured, respectively), medium (32 kW, C_2 and N_2), and high (39 kW, C_3 and N_3) torch power sprayings.

The coating porosity (estimated by image analysis and SEM at 500× on cross sections) as a function of the torch power is shown in Fig. 3. The nanocoatings exhibit higher porosity than the conventional ones when sprayed at the same power. A decrease in porosity with an increase in power is noticed for both types of coatings. For the nano-feedstock, the reduction rate of the porosity versus power is higher. It should be emphasized that the image analysis techniques can only identify the coarser pores of thermal spray coatings and give an overall view of the coating

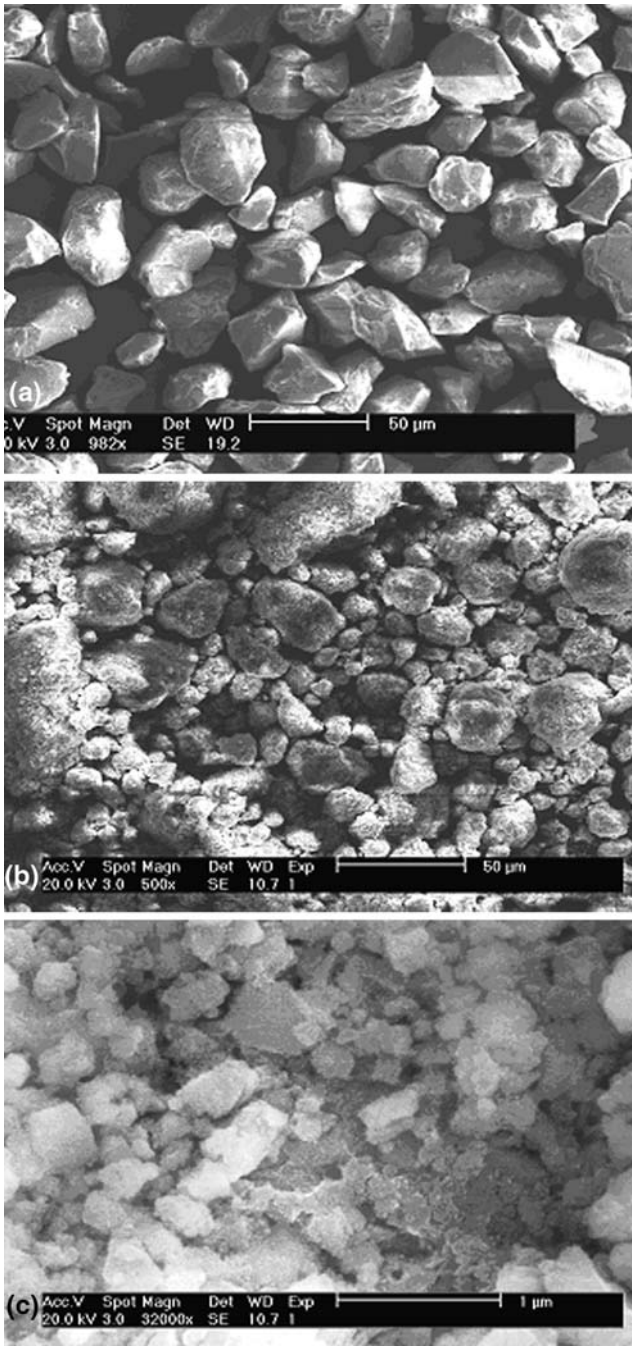

Fig. 1 SEM images of (a) CP, (b) NP, and (c) surface of the agglomerated NP particles

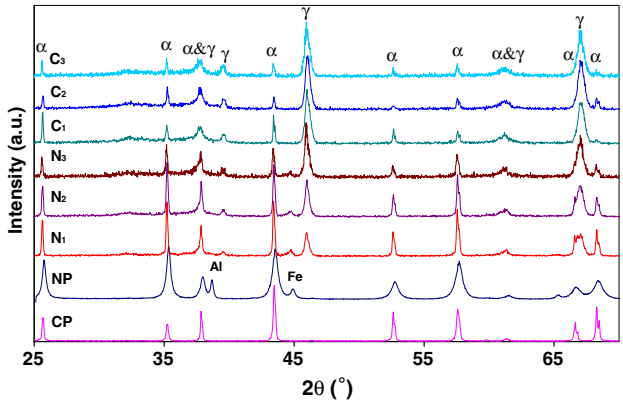

Fig. 2 XRD patterns of the initial powders and obtained coatings: α, α-Al_2O_3; γ, γ-Al_2O_3

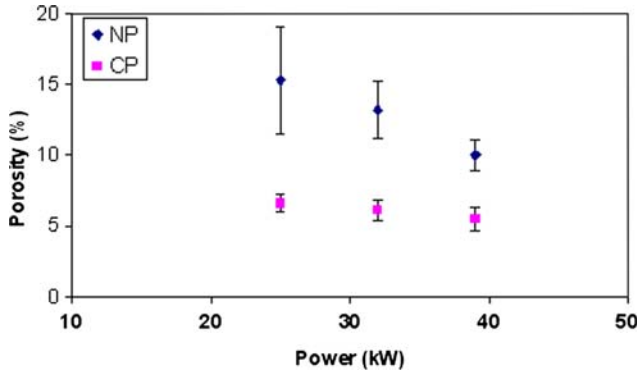

Fig. 3 The porosity for nano and conventional coatings as a function of the spray power

porosity. Mercury intrusion porosimetry (MIP) is investigated as an additional porosity calculating method for future work.

The surface state of the coatings deposited at 32 kW is illustrated in Fig. 4. The CP coatings present smoother surface than the NP coatings at all power levels, which is also verified by the surface roughness values in Table 1. The irregular/rough morphology of the nanocoatings suggests that the agglomerates retain an unmelted core. Therefore, the pile-up of the splats is not dense due to a large fraction of deposited semimolten particles, possibly accounting for the higher porosity of the nanocoatings. Similarly, the decreasing trend of roughness with torch power increasing suggests a decrease in the fraction of unmelted deposited particles and consequently an increase in the fraction of well-melted low viscosity material capable of filling the asperities of previously deposited particles. In order to verify that the agglomerated nanoparticles remain semimolten during spraying, the feedstocks were sprayed directly into deionized water.

CP and NP coatings deposited at the same torch power present similar microhardness values. Since NP coatings exhibit approximately the double porosity of the respective conventional ones, it is expected that they would have lower hardness, as the carrying load solid area is decreased (Ref 24). This contradictory result might be elaborated by two facts: first, the relatively low indentation load leads to microhardness values mostly depending on the intrinsic material properties and less depending on the material extrinsic properties, such as coarse pores, splat boundaries, etc. (Ref 25). Second, as mentioned above, the NP coatings contain a higher percentage of unmelted

material, which has retained its nano or submicron grain size. High hardness values in nanostructured materials are closely related to their low grain size, as suggested by the Hall-Petch relationship (Ref 26).

The CP coatings exhibit better adhesion than the NP coatings, as presented in Table 1. However, the adhesion value of the nanostructured coatings is considerably increased at the highest torch power (39 kW).

Figure 5(a) and (b) shows the indentation impressions on the conventional (C_3) and nanocoating (N_3) cross sections, respectively. For conventional coatings, cracks tend to propagate along splat borders parallel to the coating-substrate interface irrespectively of the torch power. No cracks or very short cracks were generated on directions vertical to the coating surface. Such an anisotropic behavior is related to accumulation of micropores between lamellae that decreases the real area of contact (Ref 27). That was not the case for the nanostructured coatings. In the NP coatings, more often crack branching was encountered. Cracks did not propagated exclusively along splat borders but were arrested or deflected along microstructure features. Such features were unmelted nanostructured areas, interfaces between fully melted and partially melted particles and pores. In Fig. 5(b), unmelted areas of retained nanostructure (marked by an arrow) are

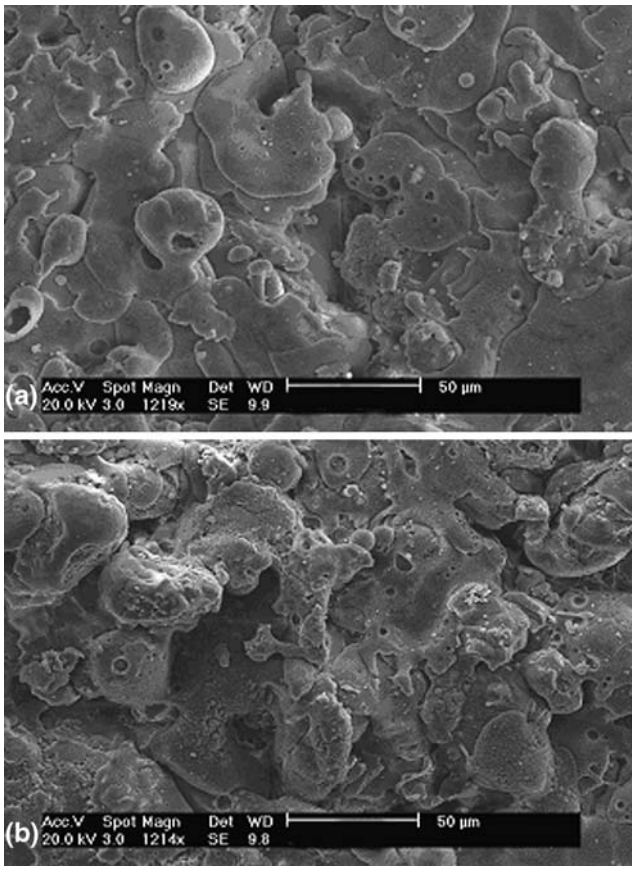

Fig. 4 The surface state of (a) CP and (b) NP coatings obtained at 32 kW spray power

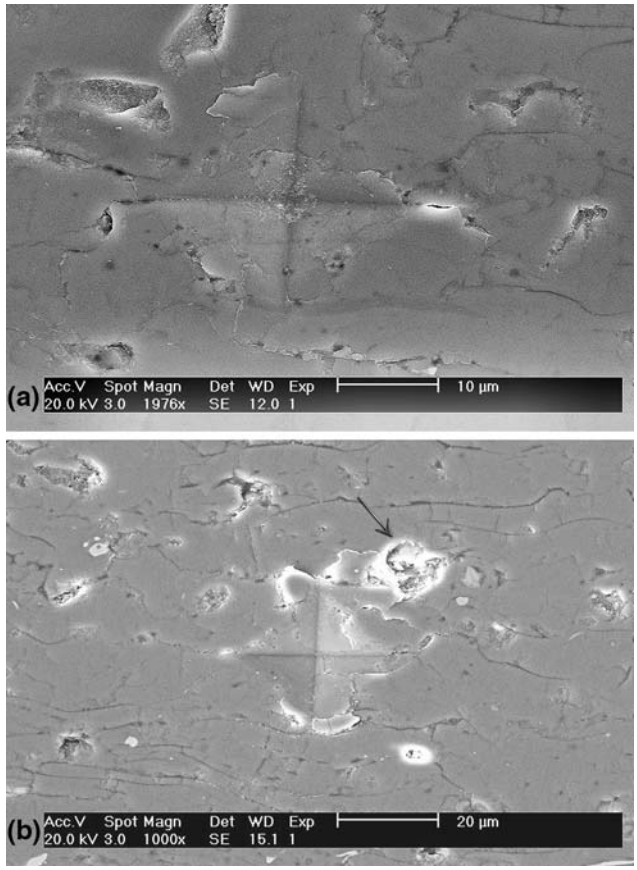

Fig. 5 The indentation impressions on coating (39 kW) cross sections. (a) CP and (b) NP; the arrow points at a crack arresting nanozone

Table 1 Coating properties

Designation	Torch power, kW	Porosity, %	Surface roughness (R_a), µm	Hardness, $HV_{100g/10s}$	Adhesion, MPa	Indentation crack length (a), µm
C_1	25	6.6 ± 0.6	7.4 ± 1.0	1063 ± 145	17.6 ± 0.9	114 ± 32
C_2	32	6.1 ± 0.7	5.9 ± 0.8	1078 ± 259	18.1 ± 1.5	78 ± 28
C_3	39	5.5 ± 0.8	5.8 ± 0.7	1147 ± 94	19.8 ± 1.6	59 ± 16
N_1	25	15.3 ± 3.8	10.2 ± 2.4	975 ± 126	10.5 ± 0.8	(b)
N_2	32	13.2 ± 2.0	10.8 ± 0.7	1070 ± 166	11.4 ± 1.3	94 ± 31
N_3	39	10.0 ± 1.1	8.4 ± 1.4	1141 ± 111	17.7 ± 2.4	55 ± 5

(a) Length of cracks at the edges of the indentation diagonal that is parallel to the coating surface
(b) Discarded measurements due to material crushing under indentation

discerned to act as crack arresters, indicating a toughening mechanism. That complicated the measurements of the cracks lengths; however, for comparison reasons, the two longest cracks propagating parallel to the coating-substrate interface were measured. For coating N_1, material crushing occurred under the indentation load due to the high level of porosity; therefore, measurements were regarded as invalid and discarded. The measured cracks for each coating are shown in Table 1. Despite the higher percentage of retained nanostructure at the lower torch powers, the higher porosity reduces fracture toughness by decreasing the solid area that carries load. However, as porosity is decreased, due to increasing torch power, and nanostructure is retained at a major fraction, a considerable increase in fracture propagation resistance is noticed.

3.3 Water-Quenched Particles

Both powders were sprayed directly into deionized water (at 39 kW) in order to investigate the mode of the melting front advance into the particle interior during their presence in the plasma stream. SEM examination shows that both water-quenched powders display a spherical microstructure; however, CP particles are compact, whereas most of the NP particles are hollow, as seen in Fig. 6 and 7, respectively. The hollow spheres consist of a dense molten wall enveloping a large void core. Since, at moderate power levels, a significant fraction of the nanoparticle agglomerates is deposited semimolten, their central voids contribute to the higher porosity (Fig. 8). As the spray power is increased, the fraction of semimolten particles is reduced, which is consistent with the rapid decrease in the porosity of the nanocoatings (Fig. 3). The higher porosity of the nanocoatings is also amplified by the low deformation ability of the semimolten particles, restricting material flow into surface asperities and irregularities of the previously deposited layer (Ref 28). Figure 9 shows that the semimolten agglomerates retain part of the initial nanostructure in the core (marked with ''1'' in Fig. 9).

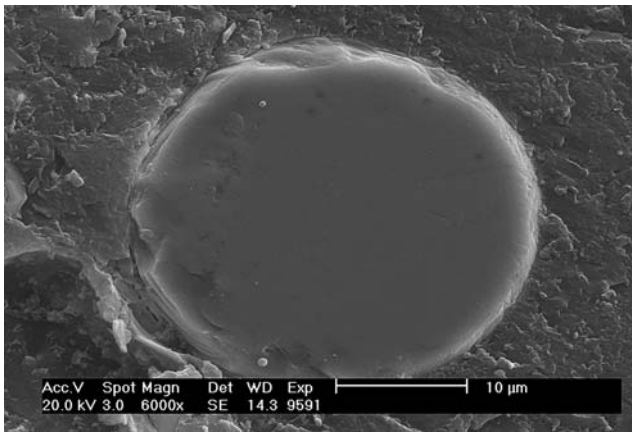

Fig. 6 CP feedstock particle, water-quenched (39 kW)

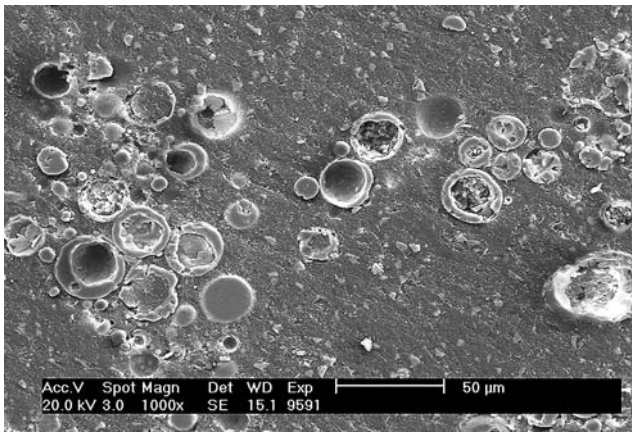

Fig. 7 NP feedstock particles, water-quenched (39 kW)

3.4 Quantitative Phase Analysis

XRD analysis (Fig. 2) shows that the deposited coatings consist of α-Al_2O_3 and γ-Al_2O_3, in compatibility with

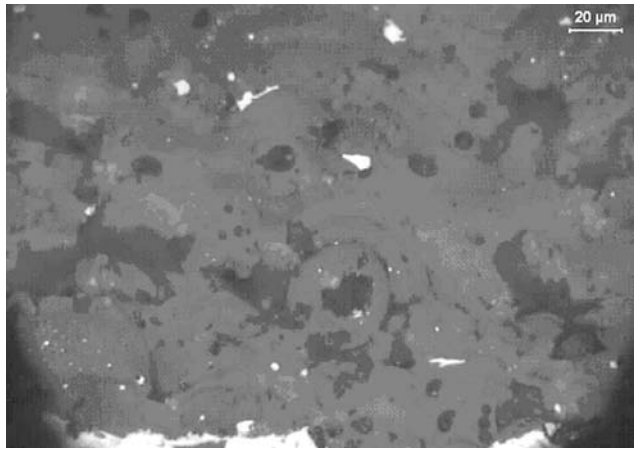

Fig. 8 Semimolten hollow spheres in the nanocoating (25 kW)

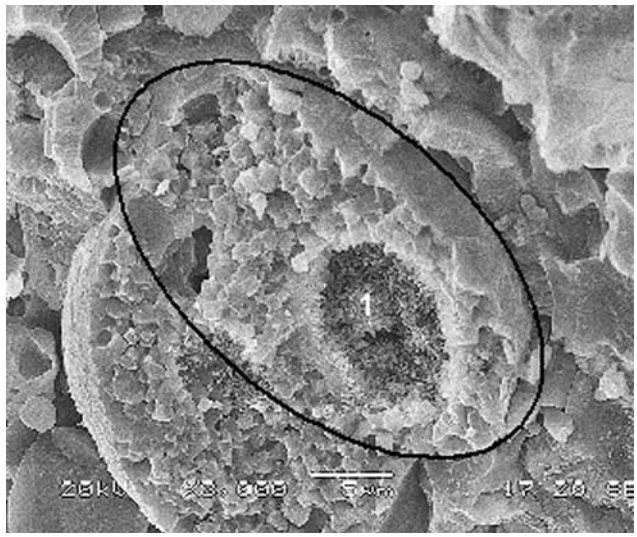

Fig. 9 Fracture surface of a semimolten particle in the nanocoating (39 kW)

previous works (Ref 8, 29). The fast cooling rates of thermal sprayed particles (10^6-10^7 K/s) can cause the stabilization of originally metastable phases. Thus, the formation of γ-Al_2O_3 in coatings is the result of rapid quench from molten Al_2O_3. α-Al_2O_3 in the coating stems from the unmelted α-Al_2O_3 fraction in the pristine powders (Ref 30).

The phase percentages for both types of coatings, as estimated by Rietveld analysis, are presented in Fig. 10. As the power increases, more γ-phase is produced, which implies that an increasing proportion of the powder particles has been melted. For the same power levels, more γ-phase is produced by the conventional powder than the nano, suggesting a higher degree of melting for the CP feedstock.

4. Discussion

During spraying, as the particles penetrate the flame, a melting front is formed that moves toward the core of the particle. As the agglomerated nanoparticles are characterized by a porous structure, air is captivated in the voids. The melting front impels the air bubbles from the voids toward the core due to the high surface tension of the molten alumina (Ref 31). This way, a central large void is developed. The formation of hollow Al_2O_3 microspheres has been attributed to the gas expansion inside the molten spheres, on temperature increasing (Ref 31).

On the other hand, conventional fused and crushed powder particles are not capable of air entrapping in their interior. Furthermore, being compact bodies, conventional particles exhibit higher thermal conductivity than their porous counterparts (Eq 2), a fact that explains their higher melting capability.

$$\lambda_p = \frac{\lambda_m}{1 + P^* \frac{\lambda_m}{\lambda_f - 1}} \quad \text{(Eq 2)}$$

where λ_p, λ_m, λ_f are the thermal conductivities of the porous coating, solid matrix, and gas (air) in the pores, respectively; P is the porosity of the coating (Ref 32).

Figures 3 and 10 indicate that a higher spraying energy is required for the nanopowder to receive porosities and phase proportions that are comparable to those obtained by spraying of the conventional powder. However, retaining part of the nanostructure is necessary for property improvement, as reported in Sect 1; too high energy levels would jeopardise this.

The decrease in the adhesion strength of the coatings (NP and CP) with spraying power decreasing is related to the respective increase in the fraction of material deposited unmelted as semimolten/unmelted particles. The large increase in the γ-fraction of the NP coatings at 39 kW may account for the large increase in the adhesion strength of the coatings deposited at this power. This energy seems sufficient to melt most of the sprayed material and increase the coating adhesion. Figure 10 shows that the N_3 coating (sprayed at 39 kW) and C_1 coating (sprayed at 25 kW) exhibit the same phase fractions, suggesting equal melting degrees. Also, Table 1 shows that the N_3 coating presents slightly lower adhesion strength than the C_1 coating. This could be related to (i) its higher porosity, as NP semimolten particles tend to form hollow spheres, and (ii) the lower cohesion of the unmelted particles compared to conventional unmelted ones, as no heat treatment of the powder was conducted prior to spraying. Figure 9 exhibits splitted semimolten particles on a fractured surface. Despite that, the N_3 coating hardness is higher than that of C_1, and taking into consideration its higher porosity, it can be claimed that its superior hardness is due to its embedded nanostructure in the coating.

Here, it should be noted that an agglomerated structure is generally expected to be more susceptible to thermal processes than a dense bulk structure, since it is a more open structure. In the present case, this did not occur (regarding the melting degree) due to the inherent porosity of the agglomerated nanoparticles and the lower thermal conductivity of captivated air in the pores as mentioned above. Related studies, confirming this, have been mentioned also elsewhere (Ref 24). NP powder manufacturing was not followed by any post-treatments,

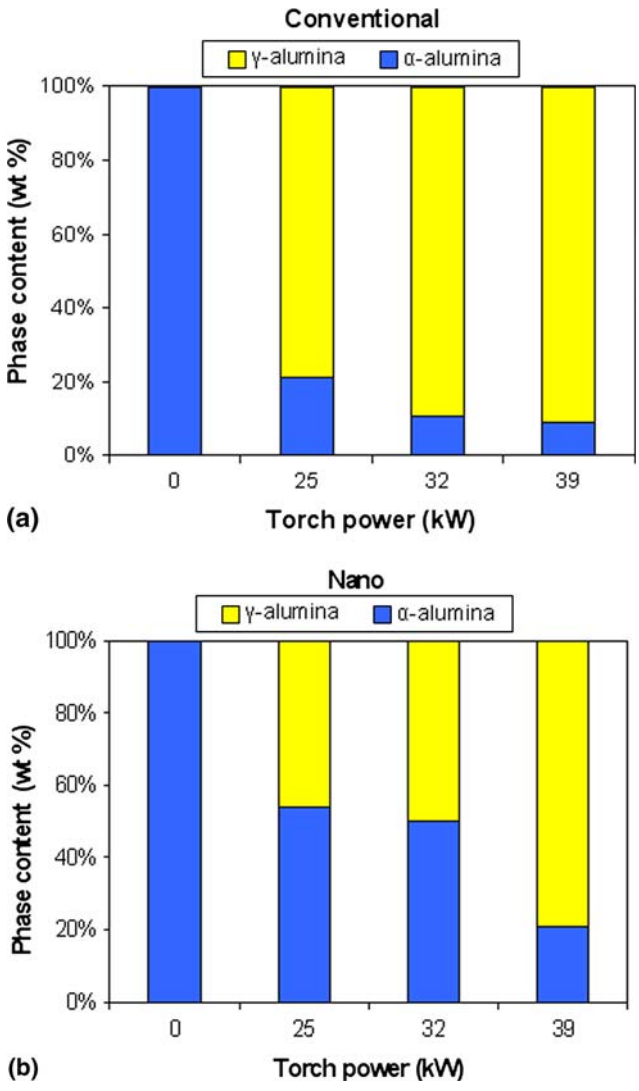

Fig. 10 Phase percentages in the coatings versus torch power

such as spray drying or sintering, which could lead to tighter structures and higher nanoparticle bond strengths (Ref 29). Sintering prior to thermal spraying was not conducted in order to avoid any grain size increase. Previous work by the authors on similar powders demonstrated that the introduction of a sintering step into the manufacturing process significantly improved the adhesion properties at all power levels (Ref 33). This improvement was attributed to sintering consequences, such as intraparticle cohesion, particle coalescence, and strain relief. Increasing particle bond strength can prevent particle dissociation when entering the plasma flame and increase the agglomerated particles density. This way, the particles may retain the momentum and access the plasma hot zone and melt more sufficiently (Ref 34).

Zones of different melting degree can be observed in the fractured surface of a semimolten particle (Fig. 9). These distinguishable zones in the particle can give information about its thermal history during its trajectory inside the plasma flame. So, from the exterior to the core of a semimolten particle, (i) complete melting of the surface has occurred that has led to γ-Al_2O_3 solidification. (ii) A liquid phase sintering zone follows formed by the flow of the molten material into the voids and the consolidation of the nanoparticles to submicron particles. This reminds of the dense nanozones described by Lima and Marple (Ref 26); though, in the present case, a major degree of consolidation has taken place, converting the nanoparticles into submicron ones. (iii) Then, a solid state sintering zone is formed, evidence that there was no sufficient time for the melt to penetrate the voids at such a distance. (iv) Finally, the central zone is free of sintering; the time and temperature were not sufficient to induce any sintering in the core, as Al_2O_3 is a moderate to bad conductor (5.9 W/mK at 1000 °C) (Ref 34).

In this work, it is possible that the thermal processes occurring during thermal spraying of the nanopowder cannot be classified into strict categories of melting or sintering, as claimed by previous researchers (Ref 28, 34). However, a combination of these may occur during thermal spraying, depending on the trajectory of the particle in a heterogeneous plasma flame, with temperature rapidly decreasing from higher than 15,000 °C (center of plasma) to ~1000 °C (end of plasma) (Ref 12).

It should be noted that the employment of this certain nano-feedstock did not yield coatings with retained nanoparticles scattered in the molten material; instead, the particles were dispersed as submicron agglomerates. However, part of the original nanograins has been retained in the central voids of the semimolten particles.

5. Conclusions

Nanostructured and conventional Al_2O_3 powders have been plasma sprayed on 304 stainless steel. The following conclusions are extracted:

1. The nanopowder consists of agglomerated nanoparticles of average size of 105 nm and lattice strain of 1.15%.
2. Less degree of melting for the nanostructured feedstock is attributed to the inherent porosity of the agglomerates.
3. The high porosity of the nanostructured coatings is partly related to the large voids formed in the interior of the semimolten particles and partly to their low deformation ability.
4. The nano and conventional coatings sprayed at the same torch power levels exhibited similar hardness values despite the higher porosity of the nanocoatings.
5. Nanostructure coatings of similar phase fractions to the conventional but with higher porosity exhibited higher microhardness due to their retained nanostructure.
6. The nano and conventional coatings displayed different crack propagation modes under indentation. The excessively increased porosity of the NP coatings plays a major role in reducing fracture toughness despite the presence of unmelted areas of retained nanostructure in the nanocoatings that can act as crack arresters. Porosity in lower levels may act beneficiary as crack arrester or crack deflector.
7. The nanocoatings demonstrated lower adhesion than conventional coatings which was related to insufficient melting and low intraparticle cohesion.
8. Increasing the torch power led to an increase in the powder melting degree and consequent decrease in the coating porosity; as a result, the coating surface roughness decreased, and the coating microhardness, adhesion strength, and fracture toughness increased with power increasing.
9. The original nanograins are mainly retained in the voids of the semimolten particles. In other parts of the structure, nanograins are consolidated to submicron particles.
10. α- and γ-Al_2O_3 proportions in the coatings are associated with the melting degree of the particles. γ-Al_2O_3 results from rapid quenching of molten particles. α-Al_2O_3 corresponds to the unmelted α-Al_2O_3 fraction in the feed powders.
11. From the periphery to the core of a semimolten particle, different structure zones can be discerned, in analogy with the transition from complete melting and rapid solidification, to liquid-state sintering, to solid-state sintering, and finally to intact areas.

Acknowledgment

D. Zois is grateful for the financial support from the Greek State Scholarships Foundation.

References

1. M. Gell, E.H. Jordan, Y.H. Sohn, D. Goberman, L. Shaw, and T.D. Xiao, Development and Implementation of Plasma Sprayed Nanostructured Ceramic Coatings, *Surf. Coat. Technol.*, 2001, **146-147**, p 48-54

2. K. Jia and T.E. Fischer, Abrasion Resistance of Nanostructured and Conventional Cemented Carbides, *Wear*, 1996, **200**, p 206-214
3. H.H. Nersisyan, H.I. Won, C.W. Won, and J.H. Lee, Study of the Combustion Synthesis Process of Nanostructure WC and WC-Co, *Mater. Chem. Phys.*, 2005, **94**, p 153-158
4. C. Berndt and E.J. Larernia, Thermal Spray Processing of Nanoscale Materials—A Conference Report with Extended Abstract, *J. Therm. Spray Technol.*, 1998, **7**, p 411-440
5. B.H. Kear and G. Skandan, Thermal Spray Processing of Nanoscale Materials, *Nanostruct. Mater.*, 1997, **8**, p 765-769
6. J. Karthikeyan, C.C. Berndt, J. Tikkanen, J.Y. Wang, A.H. King, and H. Herman, Preparation of Nanophase Materials by Thermal Spray Processing of Liquid Precursors, *Nanostruct. Mater.*, 1997, **9**, p 137-140
7. J.P. Celis, A. Basak, S. Achanta, M. Vardavoulias, and P. Mateazzi, Tribology of Nanostructured Plasma Sprayed Coatings, *2nd International Conference on Nanomaterials*, Sept 2005, Aver, Portugal, published in the proceedings
8. A. Tsetsekou, E. Tsioutsioulikli, N. Petsas, and M. Vardavoulias, Plasma Spray Coatings of Sol-Gel Ceramic Nanopowders, *20th International Conference on Surface Modification Technologies—SMT 20*, Sept 25-29, 2006, Vienna, Austria, published in the proceedings
9. Y. Zhu, M. Huang, J. Huang, and C. Ding, Vacuum-Plasma Sprayed Nanostructured Titanium Oxide Films, *J. Therm. Spray Technol.*, 1999, **8**, p 219-222
10. B.H. Kear, Z. Kalman, R.K. Sadangi, G. Skandan, J. Colaizzi, and W.E. Mayo, Plasma-Sprayed Nanostructured Al_2O_3/TiO_2 Powders and Coatings, *J. Therm. Spray Technol.*, 2000, **9**, p 483-487
11. L.L. Shaw, D. Goberman, R. Ren, M. Gell, S. Jiang, Y. Wang, T.D. Xiao, and P.R. Strutt, The Dependency of Microstructure and Properties of Nanostructured Coatings on Plasma Spray Conditions, *Surf. Coat. Technol.*, 2000, **130**, p 1-8
12. X. Lin, Y. Zeng, X. Zheng, and C. Ding, Thermal Diffusivity of Plasma-Sprayed Monolithic Coating of Alumina-3wt.% Titania Produced with Nanostructured Powder, *Surf. Coat. Technol.*, 2005, **195**, p 85-90
13. H. Chen and C.X. Ding, Nanostructure Zirconia Coating Prepared by Atmospheric Plasma Spraying, *Surf. Coat. Technol.*, 2002, **150**, p 31-36
14. E.H. Jordan, M. Gell, Y.H. Sohn, D. Goberman, L. Shaw, S. Jiang, M. Wang, T.D. Xiao, Y. Wang, and P. Strutt, Fabrication and Evaluation of Plasma Sprayed Nanostructured Alumina–Titania Coatings with Superior Properties, *Mater. Sci. Eng. A*, 2001, **301**, p 80-89
15. Y. Liu, T.E. Fischer, and A. Dent, Comparison of HVOF and Plasma-Sprayed Alumina/Titania Coatings—Microstructure, Mechanical Properties and Abrasion Behavior, *Surf. Coat. Technol.*, 2003, **167**, p 68-76
16. R.S. Lima and B.R. Marple, From APS to HVOF Spraying of Conventional and Nanostructured Titania Feedstock Powders: A Study on the Enhancement of the Mechanical Properties, *Surf. Coat. Technol.*, 2006, **200**, p 3428-3437
17. S. Eidelman and X. Yang, Three Dimensional Simulation of HVOF Spray Deposition of Nanoscale Materials, *Nanostuct. Mater.*, 1997, **9**, p 79-84
18. D. Basset, P. Mateazzi, and F. Miani, Measuring the Impact Velocities of Balls in High Energy Ball Mills, *Mater. Sci. Eng. A*, 1994, **174**, p 71-74
19. H.P. Klug and L.E. Alexander, X-Ray Diffraction Procedures, 2nd ed., Wiley, New York, 1974, p 618
20. M.E. Rabanal, A. Varez, B. Levenfeld, and J.M. Torralba, Magnetic Properties of Mg-Ferrite After Milling Process, *J. Mater. Process. Technol.*, 2003, **143-144**, p 470-474
21. C. Suryanarayana, Mechanical Alloying and Milling, *Prog. Mater. Sci.*, 2001, **46**, p 1-184
22. G.K. Williamson and W.H. Hall, X-Ray Line Broadening from Filed Aluminium and Wolfram, *Acta Metall.*, 1953, **1**, p 22-31
23. D.L. Bish and S.A. Howard, Quantitative Analysis Using the Rietveld Method, *J. Appl. Crystallogr.*, 1988, **21**, p 86-91
24. H. Luo, D. Goberman, L. Shaw, and M. Gell, Indentation Fracture Behaviour of Plasma-Sprayed Nanostructured Al_2O_3-13wt.% TiO_2 Coatings, *Mater. Sci. Eng. A*, 2003, **345**, p 237-245
25. R.S. Lima, A. Kucuk, and C.C. Berndt, Bimodal Distribution of Mechanical Properties on Plasma Sprayed Nanostructure Partially Stabilized Zirconia, *Mater. Sci. Eng. A*, 2002, **327**, p 224-232
26. R.S. Lima and B.R. Marple, Thermal Spray Coatings Engineered from Nanostructured Ceramic Agglomerated Powders for Structural, Thermal Barrier and Biomedical Applications: A Review, *J. Therm. Spray Technol.*, 2007, **16**(1), p 40-63
27. R. McPherson, A Review of Microstructure and Properties of Plasma Sprayed Ceramic Coatings, *Surf. Coat. Technol.*, 1989, **39/40**, p 173-181
28. B.H. Kear and P.R. Strutt, Chemical Processing and Application for Nanostructured Materials, *Nanostruct. Mater.*, 1995, **6**, p 227-236
29. J. Zhang, J. He, Y. Dong, X. Li, and D. Yan, Microstructure Characteristics of Al_2O_3-13wt.% TiO_2 Coating Plasma Spray Deposited with Nanocrystalline Powders, *J. Mater. Process. Technol.*, 2008, **197**(1-3), p 31-35
30. M. Wang and L.L. Shaw, Effects of the Powder Manufacturing Method on Microstructure and Wear Performance of Plasma Sprayed Alumina-Titania Coatings, *Surf. Coat. Technol.*, 2007, **202**, p 34-44
31. Z. Karoly and J. Szepvolgyi, Hollow Alumina Microspheres Prepared by RF Thermal Plasma, *Powder Technol.*, 2003, **132**, p 211-215
32. V. Hurevich, L. Smurov, and L. Pawlowski, Theoretical Study of the Powder Behaviour of Porous Particles in a Flame During Plasma Spraying, *Surf. Coat. Technol.*, 2002, **151-152**, p 370-376
33. D. Zois, A. Lekatou, M. Vardavoulias, and A. Vazdirvanidis, Nanostructured Alumina Coatings Manufactured by Air Plasma Spraying: Correlation of Properties with the Raw Powder Microstructure, ISMANAM, *15th International Symposium on Metastable, Amorphous and Nanostructured Materials*, July 6-10 2008, Buenos Aires, Argentina
34. A. Agarwal, T. McKechnie, and S. Seal, Net Shape Nanostructure Aluminium Oxide Structures Fabricated by Plasma Spray Forming, *J. Therm. Spray Technol.*, 2003, **12**, p 350-359